PHYSICAL REVIEW B **108**, 104402 (2023)

Editors' Suggestion

Spin wave Hamiltonian and anomalous scattering in $NiPS_3$

A. Scheie,[1,*,†] Pyeongjae Park,[2,3,*,‡] J. W. Villanova,[4] G. E. Granroth,[5] C. L. Sarkis,[5] Hao Zhang,[6] M. B. Stone,[5]
Je-Geun Park,[2,3,7] S. Okamoto,[8] T. Berlijn,[4] and D. A. Tennant[9,10]
[1]MPA-Q, Los Alamos National Laboratory, Los Alamos, New Mexico 87545, USA
[2]Center for Quantum Materials, Seoul National University, Seoul 08826, Republic of Korea
[3]Department of Physics and Astronomy, Seoul National University, Seoul 08826, Republic of Korea
[4]Center for Nanophase Materials Sciences, Oak Ridge National Laboratory, Oak Ridge, Tennessee 37831, USA
[5]Neutron Scattering Division, Oak Ridge National Laboratory, Oak Ridge, Tennessee 37831, USA
[6]Theoretical Division, Los Alamos National Laboratory, Los Alamos, New Mexico 87545, USA
[7]Institute of Applied Physics, Seoul National University, Seoul 08826, Republic of Korea
[8]Materials Science and Technology Division, Oak Ridge National Laboratory, Oak Ridge, Tennessee 37831, USA
[9]Department of Physics and Astronomy, University of Tennessee, Knoxville, Tennessee 37996, USA
[10]Shull Wollan Center—A Joint Institute for Neutron Sciences, Oak Ridge National Laboratory, Tennessee 37831, USA

(Received 14 February 2023; revised 28 July 2023; accepted 18 August 2023; published 1 September 2023)

We report a comprehensive spin wave analysis of the semiconducting honeycomb van der Waal antiferromagnet $NiPS_3$. Using single-crystal inelastic neutron scattering, we map out the full Brillouin zone and fit the observed modes to a spin wave model with rigorously defined uncertainty. We find that the third-nearest-neighbor exchange J_3 dominates the Hamiltonian, a feature which we fully account for by *ab initio* density functional theory calculations. We also quantify the degree to which the threefold rotation symmetry is broken and account for the $Q = 0$ excitations observed in other measurements, yielding a spin exchange model which is consistent across multiple experimental probes. We also identify a strongly reduced static ordered moment and reduced low-energy intensity relative to the linear spin wave calculations, signaling unexplained features in the magnetism which requires going beyond the linear spin wave approximation.

DOI: 10.1103/PhysRevB.108.104402

I. INTRODUCTION

Magnetic van der Waals materials which can be exfoliated down to the monolayer limit have tremendous potential for new electronics applications and devices [1]. Of special interest is whether new and exotic states can be stabilized because of the low-dimensional properties. One such candidate material is $NiPS_3$. $NiPS_3$ is a semiconducting layered honeycomb antiferromagnet with the crystal structure shown in Fig. 1. Its magnetic Ni^{2+} ions order magnetically at $T_N = 155$ K [3,4] to a zigzag antiferromagnetic order with moments along the c axis [5]. $NiPS_3$ has very strong spin-charge coupling [6,7] and because of this is already being made into workable devices [8,9]. Its magnetic excitations have been measured with powder and single-crystal neutron scattering [10,11] and density functional theory shows dominant J_3 exchange interaction [12,13], but certain features in its magnetic Hamiltonian (namely, the low-energy modes) remain imperfectly understood. Perhaps most intriguingly, x-ray, photoluminescence, and optical absorption spectroscopies show a bound exciton state consistent with Zhang-Rice triplet formation between Ni and surrounding S ligands [14], which suggests the magnetism is far from conventional. This raises two key questions: What is the full exchange Hamiltonian of $NiPS_3$, and are there signs of exotic quantum effects in the collective magnetic excitations?

To answer these questions, we perform a detailed study of single-crystal $NiPS_3$ using inelastic neutron scattering. We fit the spin waves using linear spin wave theory to estimate the magnetic exchange Hamiltonian, perform first-principles Wannier function calculations in combination with strong-coupling perturbation theory to explain this Hamiltonian, and thus derive a model which accounts for the observed excitations in optical spectroscopy [7,14]. We find a dominant third-nearest-neighbor exchange (a behavior which is unusual but fully explicable with first-principles calculations), a strongly reduced ordered moment, and anomalously small low-energy intensity. The third-nearest-neighbor exchange is fully explicable with first-principles calculations, but the reduced moment and anomalous intensity are not, and thus indicate quantum spin entanglement and higher-order effects.

II. EXPERIMENT AND RESULTS

We measured the inelastic neutron scattering spectrum of $NiPS_3$ using the SEQUOIA spectrometer [15,16] at the Spallation Neutron Source (Oak Ridge National Laboratory) [17]. The sample consisted of 26 coaligned crystals (total 2.41 g) glued to aluminum plates with the c axis vertical (see

---

[*] These authors contributed equally to this work.

[†] scheie@lanl.gov

[‡] ppj0730@snu.ac.kr

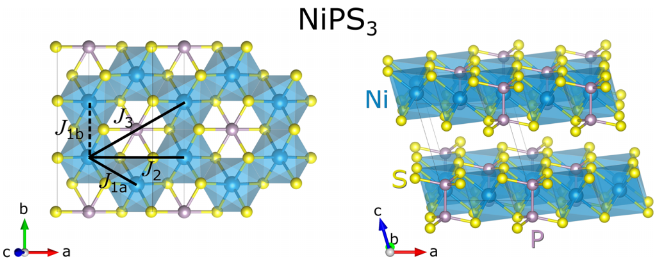

FIG. 1. Crystal structure of NiPS$_3$, shown for a single layer (left) and the stacking pattern for multiple layers (right) visualized using VESTA [2]. The first three neighbor in-plane exchanges are shown on the left.

Appendix A for details). Although NiPS$_3$ technically has broken threefold rotation symmetry at the Ni^{2+} sites, the distortion is so weak that we could not easily distinguish (h00) from (hh0), and in the coalignment we treated them as identical. In the plots in this paper, the cuts listed (e.g., in Fig. 2) in reality include a superposition of cuts rotated in the plane by ±120°. (In the spin wave modeling below, we calculated the three overlapping orientations with a weighting 1:1:1.) For a background, we measured an identical sample holder with no sample. We measured the inelastic spectra in the (hk0) scattering plane with incident energies (E_i) of 28, 60, and 100 meV at 5 K, and $E_i = 28$ meV and $E_i = 100$ meV at 100 K, and 200 K. Data were then symmetrized by in-plane reflections about ($h0\ell$) and ($0k\ell$). Two-dimensional slices of scattering data are shown in Fig. 2.

In the 5- and 100-K data, spin wave modes are clearly visible in the data, being very well defined in the in-plane scattering directions, with a pronounced maximum intensity at ∼14 meV. At 200 K (above $T_N = 155$ K), the modes are less well defined and the gap closes. The most intense inelastic scattering is at the bottom of the dispersion at k and h wave vectors associated with the zigzag antiferromagnetic order. This mode has very steeply dispersing magnon modes which, because of experimental resolution broadening, makes the low-energy extent difficult to experimentally determine. Nevertheless, as temperature increases, the gap steadily closes (Fig. 3). This temperature-dependent gap is well understood for low-dimensional magnets [18], and was also observed in FePS$_3$ [19] and MnPS$_3$ [20].

Although experiments clearly show NiPS$_3$ to be dominated by in-plane exchange interactions, a weak dispersion is visible in the ℓ (out-of-plane) direction as shown in Fig. 2(d). Because of the intense, highly dispersive scattering, the ℓ dependence appears as a lower envelope to the scattering with a bandwidth of 6.5 meV. The ℓ periodicity is the same as the lattice, indicating ferromagnetic interplanar exchange.

III. SPIN WAVE FITS

Having observed such well-defined magnons, we fitted a linear spin wave theory (LSWT) model to the data to determine the exchange constants. However, we must also ensure that our model is consistent with other experiments. From other studies, it is clear that the Ni^{2+} magnetism is predominantly easy plane [3,12,21,22]. In addition, multiple measurements have reported three low-energy $Q = 0$ magnetic modes in the NiPS$_3$ ordered phase: Electron spin resonance indicates $\Delta_1 = 1.07$ meV [22], optical spectroscopy indicates $\Delta_1 = 1.16$ meV and $\Delta_2 = 3.79$ meV [7], and photoluminescence indicates $\Delta_1 = 1.7$ meV and $\Delta_2 = 3.3$ meV, deduced from shoulder peaks near the main photoluminescence peak (proposed to be the Zhang-Rice singlet to Zhang-Rice triplet transition) [14]. Meanwhile, terahertz optical spectroscopy reveals a clear $Q = 0$ magnon mode at

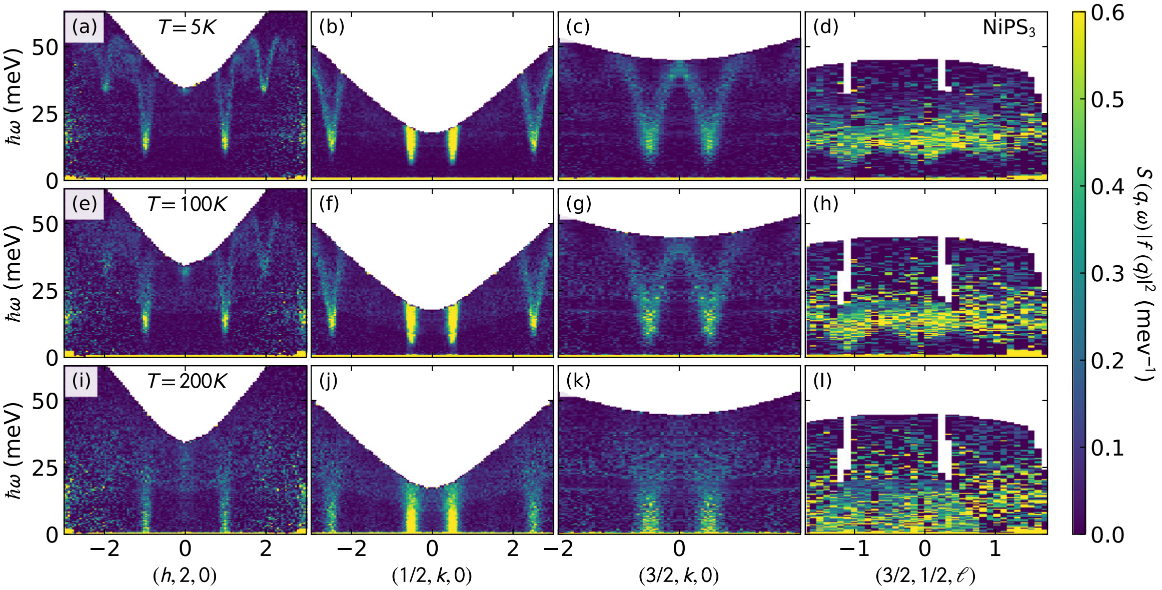

FIG. 2. Measured neutron spectra of NiPS$_3$ along different directions in reciprocal space. Data at [(a)–(d)] 5 K, [(e)–(h)] 100 K, and [(i)–(l)] 200 K. In each panel, the different E_i data are overlaid. The boundaries between the different data sets appear as faint grey lines. At 5 and 100 K, spin wave modes are clearly visible. The modes become broadened and gapless at 200 K. Note that all data are symmetrized about $h = 0$ and $k = 0$, and intensity is in absolute units but not corrected for the form factor.

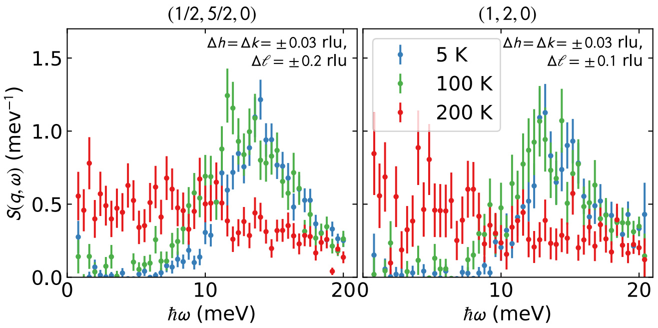

FIG. 3. Temperature evolution of the low-energy gapped mode in NiPS$_3$, showing (1/2, 5/2, 0) and (1,2,0) wave vectors measured with $E_i = 28$ meV neutrons. Between 5 and 100 K, the intensity maximum shifts slightly lower in energy, while at 200 K (above T_N) the modes become gapless. Note that the intensity profiles of the two points (which nominally correspond to C and Γ) are identical, even with different ℓ integration widths.

$\Delta_3 = 5.5$ meV which disappears as $T \to T_N$ and is also present in the absence of photoexcitation [23]. By semiclassical spin wave theory, there can only be two low-energy $Q = 0$ modes in NiPS$_3$. We believe the true $Q = 0$ magnons are Δ_1 and Δ_3 because the $\Delta_2 \approx 3.5$ meV mode only appears with >1 eV optical pumping and is near $2\Delta_1$, suggesting it is a nonequilibrium effect and/or involves the creation of two low-energy magnons. [One other possibility is a longitudinal magnon mode, but $SU(3)$ simulations do not find an additional mode, (see Appendix D). Furthermore, longitudinal modes are typically far broader in energy than the transverse magnons [24], not sharp modes as observed in NiPS$_3$.) Thus, we take the low-energy $Q = 0$ magnon gaps to be $\Delta = (1.3 \pm 0.3)$ meV (average of the reported values) and $\Delta = (5.5 \pm 0.3)$ meV (uncertainty taken from the lower-energy mode). We include these fixed average gap values in our model for the low-energy $Q = 0$ modes.

The fitted model is based on Heisenberg (isotropic) exchange with single-ion anisotropy terms,

$$\mathcal{H} = \sum_{ij} J_{ij} \mathbf{S}_i \cdot \mathbf{S}_j + \sum_i \left[A_x \left(S_i^x\right)^2 + A_z \left(S_i^z\right)^2 \right], \qquad (1)$$

where $\mathbf{S}_i$ are quantum spin operators of length 1, J_{ij} determine the exchange interaction strengths, and A_x and A_z are the single-ion anisotropy terms. To constrain the fit, we extracted the spin wave dispersions from the neutron data by fitting multiple independent constant-Q cuts with a Gaussian across 18 different $\hbar\omega$ vs Q slices (see the Supplemental Material [25]). Where the dispersion was steep, we also fitted constant $\hbar\omega$ slices, yielding a total 267 individual Q and $\hbar\omega$ points (treating data from each different measured E_i separately). We then fit the NiPS$_3$ spin waves to the mode energies using SPINW [26] assuming three in-plane exchanges and one out-of-plane exchange J_4. We found that, in order to produce a $q = K = (1/2, 1/2, 0)$ intensity maximum at ∼14 meV while retaining the two low-energy $Q = 0$ modes above, the threefold rotation axis must be weakly broken (which, as shown in Fig. 1, is true of the $C2/m$ space group for NiPS$_3$). Otherwise, the only modes at $q = K$ would be $\Delta = 1.3$ meV and $\Delta = 5.5$ meV. We therefore allow the two symmetry-inequivalent first-neighbor bonds to have different values (J_{1a} and J_{1b}), while the other in-plane exchanges J_2 and J_3 are assumed to have the same exchange on all honeycomb bonds. The resulting fitted parameters are in Table I, with the linear spin wave simulated scattering in Fig. 4. A plot of high-symmetry cuts is shown in Fig. 5. (See Appendix B for the uncertainty estimation method, and note that although J_{1a} and J_{1b} individual uncorrelated uncertainties overlap, $J_{1b}/J_{1a} > 1$ to within uncertainty.)

TABLE I. Hamiltonian exchange parameters for NiPS$_3$. The left column shows the best fit model in units of meV, where the broken threefold symmetry is represented by J_{1a} (two nearest-neighbor exchanges with components along the a axis) and J_{1b} (nearest-neighbor exchange along the b axis). Error bars indicate one standard deviation uncertainty. The right column shows the density functional theory (DFT) calculated exchange constants for J_1, J_2, and J_3, which are very close to the experimental values.

Model	Fitted LSWT	DFT + perturbation ($U = 3$ eV, $J_H = 0.5$ eV)
A_x	-0.010 ± 0.005	
A_z	0.21 ± 0.03	
J_{1a}	-2.7 ± 0.4	-2.7
J_{1b}	-2.0 ± 0.4	-2.4
J_2	0.2 ± 0.3	-0.42
J_3	13.9 ± 0.4	13.9
J_4	-0.38 ± 0.05	

One thing that was immediately apparent was that—even assuming a broken threefold rotation symmetry—there was far too much intensity at low energies for all our initial LSWT simulations [Figs. 4(f)–4(j)]. However, we found that if we calculated the LSWT over a finite window in Q transverse to match the experimental bin widths [±0.05 reciprocal lattice units (RLU) in the plane, and ±0.25 RLU out of the plane], we reproduced the low-energy modes better [Figs. 4(k)–4(o)], though not perfectly as we discuss below. The dispersion is so steep there that any finite bin size broadens the modes and shifts the intensity maximum to higher energy transfers. This explains the anomalous intensity down to very low energies at the antiferromagnetic wave vectors also observed in Ref. [11]. This also meant that the fitted experimental Q and $\hbar\omega$ points, because they were extracted from cuts with finite bin size, are higher than the actual modes. We therefore calculated the difference in mode energy between the raw LSWT calculation [Figs. 4(f)–4(j)] and the finite-bin summed LSWT calculation [Figs. 4(k)–4(o)], corrected the experimental Q and $\hbar\omega$ points by this offset, and refit the Hamiltonian. The values in Table I represent the fit to these corrected dispersions.

In fitting the Hamiltonian, we also included in-plane exchange terms beyond the third-nearest neighbor in plane, but we found that these did not improve the reduced χ^2 by $\geqslant 1$, and thus we consider them to be zero to within uncertainty. We also tried including a Kitaev term in the exchange, but this also did not improve the fit and instead introduced extra modes in the spectrum which are not present in experiment. Finally, we note that in reality, the broken rotation symmetry will affect all bonds, not just J_1. However, to reduce the number of fitted parameters, we collect all such effects in J_1 in order to provide a minimal model for reproducing the experimental observations.

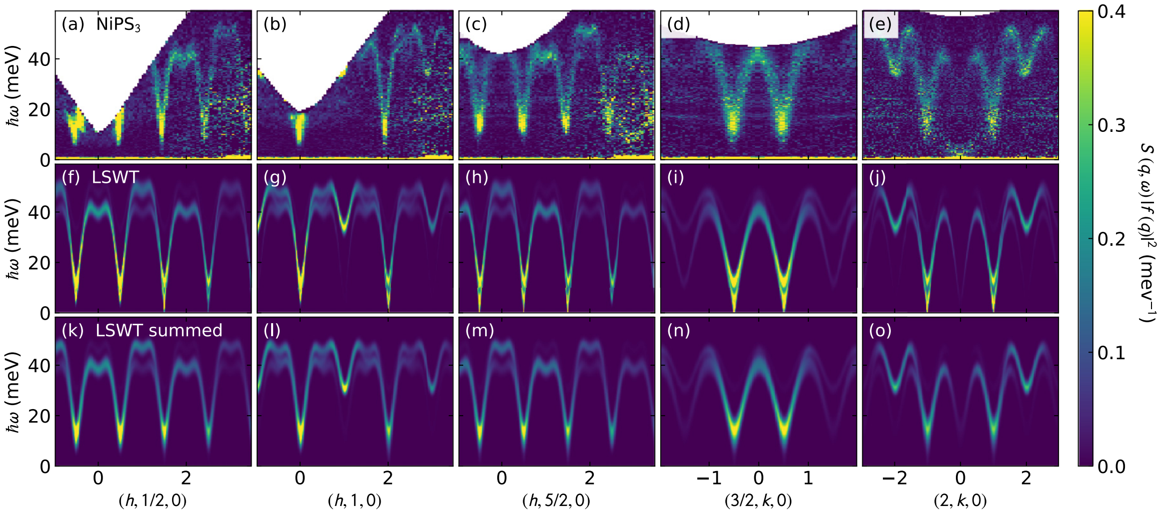

FIG. 4. Measured and fitted NiPS$_3$ spin wave spectra. [(a)–(e)] The measured spin wave spectra (with $E_i = 100$, 60, and 28 meV overlaid as in Fig. 2). [(f)–(j)] The fitted linear spin wave theory (LSWT) spectra and [(k)–(o)] the same LSWT spectra integrated over the finite widths in h, k, and ℓ for the actual experimental data. Because of finite bin widths, the low-energy scattering is much weaker than it would be with infinitesimal bins. (Note that the low-energy intensity in panel (e) near (200) is an acoustic phonon mode.)

One of the most striking features of the fit is that the third-nearest-neighbor exchange J_3 dominates the Hamiltonian. A dominant third-nearest-neighbor in-plane exchange is not unusual for hexagonal 3d magnets, as seen in, e.g., NiGa$_2$S$_4$ [27], Ba$_2$NiTeO$_6$ [28], Na$_2$Co$_2$TeO$_6$ [29], BaNi$_2$(AsO$_4$)$_2$ [30], and BaCo$_2$(AsO$_4$)$_2$ [31] and many members of the MPX_3 family [32–34]. However, the extremely large J_3 we derive (nearly six times larger than J_1, or $|J_3/\bar{J}_1| = 5.9$) is, to our knowledge, the largest observed.

IV. FIRST-PRINCIPLES CALCULATIONS

A. Density functional theory

To explain this enormous J_3, we perform density functional theory (DFT) calculations to estimate the Hamiltonian from first principles. Reference [33] studied Dirac cones formed by the half-filled e_g bands in monolayer MBX_3, focusing on monolayer PdPS$_3$. They plotted the monolayer Wannier functions and reported the hopping integrals to neighboring transition metal sites. Likewise, we justify the hierarchy of magnetic exchange constant magnitudes by examining the respective hopping integrals of the e_g bands first. The maximum magnitude of the nearest-, second-nearest-, and third-nearest-neighbor hopping integrals are 52.94, 29.54, and 215.52 meV, respectively (see also Table IV). The e_g-e_g hopping integrals for nearest neighbors are relatively small, and they are even surpassed by the e_g-t_{2g} hopping integrals ($52.94 < 176.01$ meV). The present calculation for bulk NiPS$_3$ is distinct from the monolayer calculation of Ref. [33] in that it incorporates the t_{2g} orbitals, and their relative importance for the nearest-neighbor exchange is already evident. Next we explain why the inclusion of the t_{2g} orbitals is necessary to capture ferromagnetic (FM) exchange for the nearest neighbors [failure to do so inaccurately leaves one with an antiferromagnetic (AFM) J_1 and overestimates J_3] and examine how the large third-nearest-neighbor hopping integral comes to be.

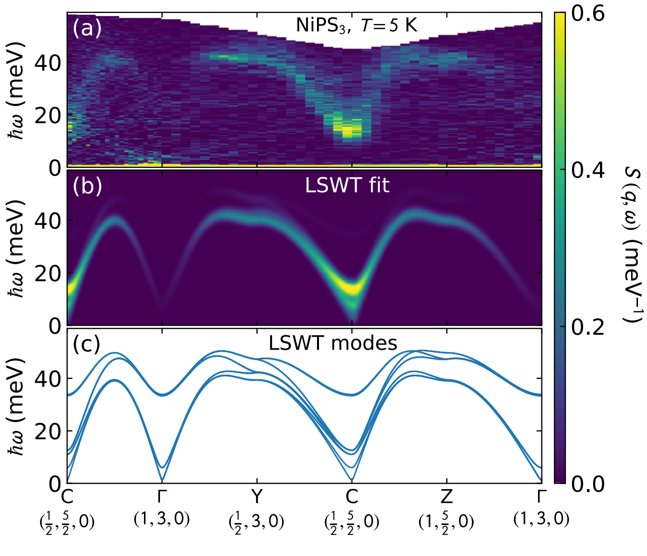

FIG. 5. Plot of (a) scattering data along high-symmetry directions compared to (b) the linear spin wave theory (LSWT) simulation and (c) the LSWT mode energies.

We visually demonstrate how the hopping integrals are either notable or diminished in Fig. 6. The third-nearest-neighbor (3NN) e_g-e_g hopping integrals are the largest of all, leading to the large AFM 3NN exchange. Previous work has argued for substantial overlap to produce the d-p-p-d exchange for the e_g orbitals for 3NN hopping [33,35] and this is shown in Fig. 6(a). The 3NNs do not share ligand S atoms, and the p-tail lobes point toward each other, further enhancing overlap. By contrast, the nearest-neighbor (1NN) e_g-e_g hopping integrals are relatively diminished, leading to small FM 1NN exchange. As shown in Fig. 6(d), the orientation of the p tails on the shared ligand S atoms is nearly orthogonal, leading to substantial cancellation.

The e_g-t_{2g} hopping integrals are important both to capture the FM nature of the 1NN exchange and to accurately

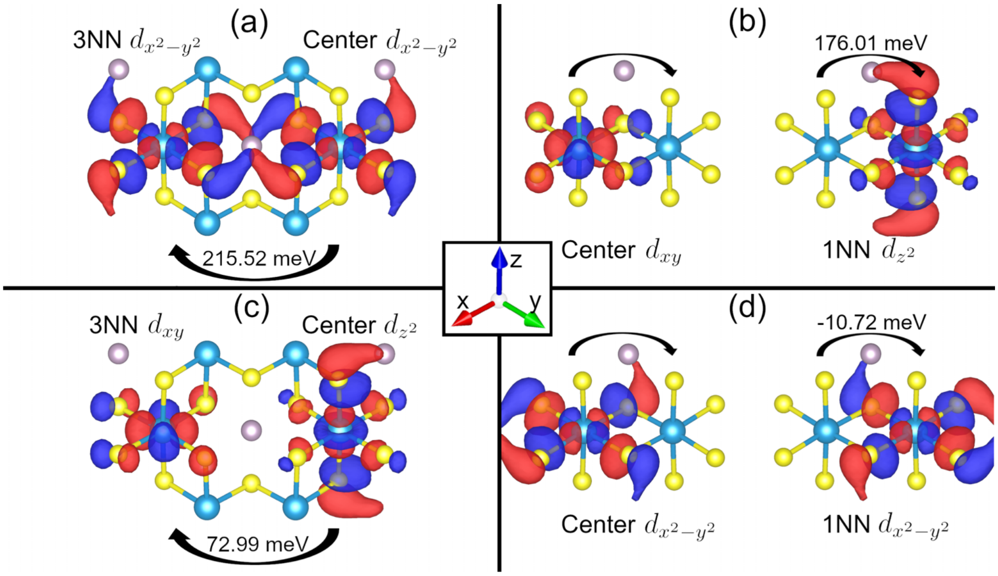

FIG. 6. Wannier function overlaps. (a) The largest hopping integral for the third-nearest neighbor (3NN) between $d_{x^2-y^2}$ orbitals. (b) The largest hopping integral for the nearest neighbor (1NN) between d_{xy} and d_{z^2} orbitals. (c) The second largest hopping integral between 3NN d_{xy} and d_{z^2} orbitals. (d) The diminished hopping integral between 1NN $d_{x^2-y^2}$ orbitals. Red (blue) surfaces are the positive (negative) isosurfaces. Teal atoms are Ni, grey atoms are P, and yellow atoms are S (like Fig. 1).

calculate the 3NN exchange. Figure 6(b) shows the 1NN overlap between d_{xy} and d_{z^2} orbitals. Again, the 1NNs share their ligand S atoms, but the p tails overlap each other to reinforce the hopping. In Fig. 6(c), the 3NN overlap between d_{xy} and d_{z^2} orbitals is relatively diminished; the d_{z^2} orbital's primary p tails are not pointing toward the neighboring Ni atom, and the smaller p tails point toward each other less directly than in the e_g-e_g case. This e_g-t_{2g} process contributes to FM 3NN exchange, but it is merely a small fraction of the large AFM exchange supported by the e_g-e_g hopping.

B. Perturbation theory

Armed with the full e_g and t_{2g} tight-binding Hamiltonian, we apply perturbation theory in the strong-coupling limit (explained in Appendix E) to extract the exchange constants, listed in Table I. These are in close agreement with the experimentally fit exchange constants, except for the theoretical prediction that J_2 be weakly ferromagnetic where it is experimentally shown to be weakly antiferromagnetic. Our perturbation theory results are also in close agreement with the results in Ref. [13] obtained from fitting total energies of magnetic configurations simulated with DFT+U.

The theoretical prediction can be understood as follows. For a given pair of atoms, there are three major exchange processes to consider, one FM interaction and two AFM interactions as depicted in Fig. 7. The (1) FM and (2) first AFM processes involve e_g-t_{2g} hopping, and (3) the other AFM process involves e_g-e_g hopping. The difference between the former two processes is in the intermediate states which arise in the calculation of the second-order perturbation to the energy. The intermediate state of FM process 1 maximizes the spin multiplicity (total spin quantum number) on one atom (in comparison to AFM process 2), giving a lower Hund energy for that configuration, and thus a larger reduction in the energy. FM process 1 tends to dominate for reasonable values of the interaction parameters. For the results in Table I we used $U = 3$ eV and $J_H = 0.5$ eV. See Appendix E for the full dependence on U and J_H.

Thus, for the nearest neighbors where the strongest hopping is e_g-t_{2g}, the FM exchange process dominates and $J_1 < 0$. For the second-nearest neighbors, the strongest hopping is again e_g-t_{2g}, and again the FM process dominates, but the maximum magnitude of these hopping integrals is less than half that of the nearest neighbors. So again $J_2 < 0$ (theoretically, and maybe experimentally to within uncertainty), but it

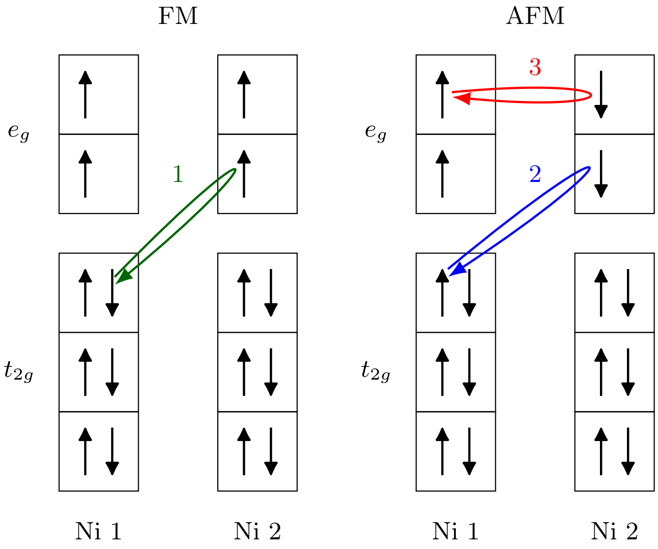

FIG. 7. Schematic diagram of the major ferromagnetic and antiferromagnetic exchange processes in the e_g and t_{2g} band manifolds. The boxes indicate electron orbitals, and the loops indicate hopping pathways.

is less than one-quarter the magnitude of the nearest-neighbor exchange. Finally for the third-nearest neighbors, the e_g-e_g AFM process is by far the dominant exchange and $J_3 > 0$, with the largest magnitude of all the exchange constants. The third-nearest-neighbor d_{z^2}-d_{xy} hopping integral is not negligible (Table VI), so the competition between FM process 1 and AFM process 2 is still present, but this cannot overpower the e_g-e_g AFM process for which the hopping integral is three times larger. However, this does indicate that a model including only the e_g-e_g AFM process will overestimate the large J_3.

V. DISCUSSION

At this point, we have a theoretical model for the observed spin waves and $Q = 0$ excitations, as well as a first-principles explanation for the strength of the exchange couplings. Thus we have answered our first question about the $NiPS_3$ exchange Hamiltonian. Now we turn to the second question: Given the proposed exotic Zhang-Rice behavior of $NiPS_3$, are there any features in the inelastic spectrum which *cannot* be accounted for by linear spin wave theory?

Although the LSWT calculation reproduces the inelastic spectrum well, the LSWT approach does not match the static ordered moment. Antiferromagnetic spin waves will, in general, reduce the size of the ground state ordered moment relative to its maximum value [36], and substantial quantum entanglement can reduce the moment much further. Calculating the $T = 0$ spin expectation value for the fitted spin wave Hamiltonian, we find $g\langle S\rangle = 1.73\mu_B$ (assuming $g = 2.00$) for Ni^{2+}. This is much larger than the experimental ordered moment $1.05\mu_B$ [5], which indicates that the real material $NiPS_3$ has substantially more quantum fluctuations than linear spin wave theory gives.

In general, a strongly reduced static $T \to 0$ moment (formally defined by the "one-tangle" entanglement witness [37]) indicates substantial quantum spin entanglement, showing that $NiPS_3$ is not merely a conventional antiferromagnet. In other words, the Ni^{2+} magnetism cannot be described by linear spin wave theory alone, and therefore it is subject to more exotic quantum effects. The missing spin components presumably reside within the excitation spectrum, potentially at $Q = 0$ where neutrons cannot directly probe.

The next item of comparison is details in the neutron spectrum. We compare the experimental data against resolution-convolved simulated scattering from best fit parameters in Table I using MCVINE, a Monte Carlo ray tracing software to simulate time-of-flight resolution effects for the exact instrumental configuration and experimental bin widths [38,39] as shown in Fig. 8 (see Appendix C for details).

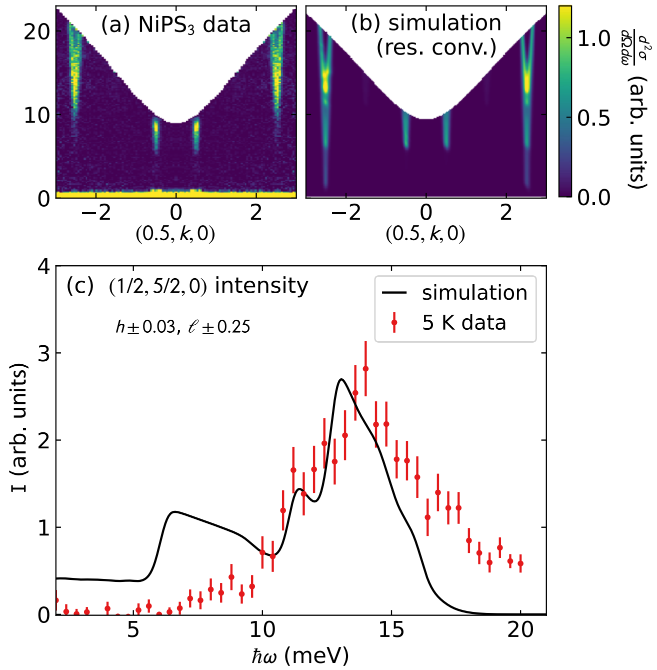

FIG. 8. Comparison between simulated resolution-broadened spin waves and experimental data at the bottom of the dispersion. (a) The $E_i = 28$ meV data at 5 K, and (b) the exact same cut with the best fit Hamiltonian LSWT simulation with MCVINE simulated resolution convolution. The intensity maxima in experiment and theory are close in energy, but the theoretical intensity extends much lower in energy. (c) A constant-Q plot of experiment and simulation, showing that the experimental low-energy tail of the dispersion is suppressed relative to the LSWT calculation.

Although LSWT correctly captures the intensity near the finite-energy maximum, LSWT predicts a much larger low-energy "tail" to the dispersion than is seen experimentally. In Appendix D we show that quadrupolar $SU(3)$ dynamics (as will be present in $S = 1$ Ni^{2+} [40]) explains one-third of the reduced intensity, but nowhere near the dramatic reduction seen in experiment. The absent intensity must have a more exotic explanation. It is striking that the intensity is anomalously small at the lowest energies, near where the $\hbar\omega = 0$ static magnetism is also anomalously small. This means that quantum effects somehow seem to suppress the low-energy (long-time) magnetic response in $NiPS_3$.

The combination of a reduced static moment and anomalously suppressed low-energy intensity shows that LSWT fails to fully account for the low-energy magnetism of $NiPS_3$. Further theoretical modeling is required to say for certain whether Zhang-Rice triplets account for the reduced moment, but we propose the observed resonances in Ref. [14] as a potential explanation. A careful measure of the magnetic form factor could indicate whether a portion of the magnetic moment resides on the S sites in accord with the Zhang-Rice triplet hypothesis. Be that as it may, these experimental observations beg for theoretical explanation: Something very unusual is going on at the lowest energies. $NiPS_3$ has conventional magnons, but that is not the end of the story.

VI. CONCLUSION

We have measured the spin wave spectrum in $NiPS_3$ and modeled the spin waves, extracting a magnetic Hamiltonian with rigorously defined uncertainty. We have also used first-principles calculations to model the magnetic exchange, and we find that DFT agrees very well with our experimentally determined exchange constants—in particular the anomalously large third-nearest-neighbor exchange J_3. The microscopic mechanism for the dominant third-nearest-neighbor exchange is elucidated by combining DFT with strong-coupling perturbation theory. Our fitted model is able to account for the finite energy maxima observed in neutron scattering, as well as the mode gaps observed in other experimental methods. The full profile we provide of long-wavelength ($Q = 0$) magnetic excitations is essential knowledge for van der Waal magnets, because these modes most directly couple to optical and electronic excitations as relevant for spin-orbit entangled excitons and spintronic technology.

Finally, we highlight a dramatically reduced static moment and suppressed low-energy intensity, which indicates that LSWT fails to fully explain $NiPS_3$ magnetism, especially in the low-energy (long-time) dynamics. This indicates an anomalous quantum state in $NiPS_3$, potentially driven by Zhang-Rice triplet pairing.

Note added. Recently, Ref. [11] was published reporting similar measurements and a similar fitted spin exchange Hamiltonian to this study.

ACKNOWLEDGMENTS

This research used resources at the Spallation Neutron Source, a U.S. Department of Energy (DOE) Office of Science User Facility operated by the Oak Ridge National Laboratory (ORNL). The work by A.S., J.W.V., C.L.S., and D.A.T. is supported by the Quantum Science Center (QSC), a National Quantum Information Science Research Center of DOE. S.O. is supported by the U.S. Department of Energy, Office of Science, Basic Energy Sciences, Materials Sciences and Engineering Division. Part of this research (T.B.) was conducted at the Center for Nanophase Materials Sciences, which is a DOE Office of Science User Facility. Work on the resolution calculations was funded by the Laboratory Directors' Research and Development Fund of ORNL. The resolution calculations also used resources of the Compute and Data Environment for Science (CADES) at the Oak Ridge National Laboratory, which is supported by the Office of Science of the U.S. Department of Energy under Contract No. DE-AC05-00OR22725. The work at SNU was supported by the Leading Researcher Program of Korea's National Research Foundation (Grant No. 2020R1A3B2079375). H.Z. gratefully acknowledges the support of the U.S. Department of Energy through the LANL/LDRD Program and the Center for Non-Linear Studies. The authors acknowledge helpful discussions with Christian Batista.

APPENDIX A: SAMPLE PREPARATION AND EXPERIMENTAL DETAILS

Single-crystal $NiPS_3$ was grown by a standard chemical vapor transport method. Pure Ni (>99.99%), P (>99.99%), and S (>99.998%) powders were mixed in a molar ratio of 1:1:3 inside an Ar-filled glove box. We added an additional 5% sulfur to the mixture for vapor transport. We analyzed the chemical composition of the resultant single crystals using energy-dispersive x-ray spectroscopy (Bruker QUANTAX 70), which confirmed a correct stoichiometry. We further characterized its magnetic property using a commercial SQUID magnetometer (MPMS-XL5, Quantum Design), the result of which is consistent with previous studies [5,21].

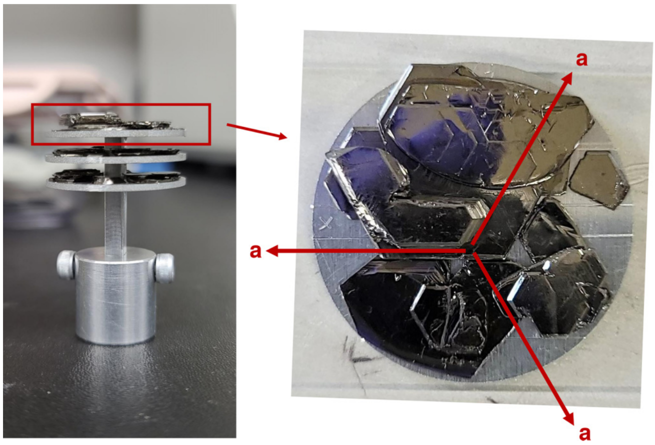

FIG. 9. $NiPS_3$ sample mount, shown from the side and from the top. Because of the near-threefold rotation symmetry, the coaligned crystals are aligned with the a axis in one of three directions, as shown on the right.

The sample for the SEQUOIA experiment was composed of several coaligned $NiPS_3$ crystals totaling 2.41 g, glued to aluminum plates with CYTOP glue [41]. The sample mount in shown in Fig. 9. Because of the near-threefold rotation symmetry about $\mathbf{c}^*$ and the weak interplane van der Waals bonding, the sister compound $FePS_3$ has twinned domains separated by 120° rotation about $\mathbf{c}^*$ [42,43], and we expect the same situation with $NiPS_3$. Indeed, x-ray Laue diffraction failed to distinguish the [100] from the $[-1/2, 1/2, 0]$ or $[-1/2, -1/2, 0]$ directions, which meant that the sample is a combination of orientations as shown in Fig. 9.

The instrument settings for the SEQUOIA neutron measurements are given in Table II. For background, we made an identical sample holder with the same amount of CYTOP glued to it but with no crystals. This dummy sample was measured at the same energy and temperature configurations as the actual sample, and the measured scattering intensity was subtracted from the data. Plotted data were symmetrized with the following symmetry operations: x, y, z; $-x, y, z$; $x, -y, z$; $-x, -y, z$ (see Fig. 10).

Data were normalized to absolute units by fitting the (060) transverse acoustic phonon in accord with Ref. [44] as shown in Fig. 11. Data were normalized per formula unit, equivalent to per Ni ion.

TABLE II. SEQUOIA instrument parameters [16] for the $NiPS_3$ spin wave measurements at the various incident energies. Fermi Chopper 2 (middle column) is the high-resolution chopper.

Nominal E_i (meV)	Actual E_i (meV)	Fermi Chopper	Fermi ν (Hz)	T_0 ν (Hz)
100	103.4	2	540	120
60	62.1	2	420	90
28	28.9	2	300	60

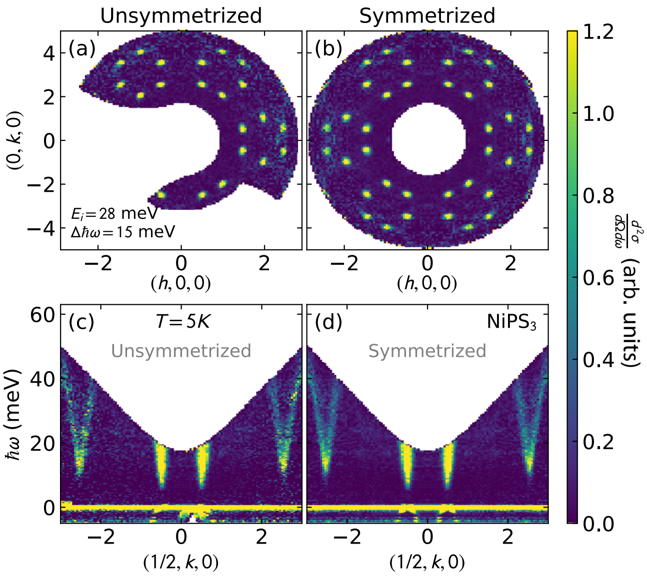

FIG. 10. Symmetrization of NiPS$_3$ neutron data. The left column shows the unsymmetrized data, and the right shows the symmetrized data $(x, y, z; -x, y, z; x, -y, z; -x, -y, z)$ for a constant-energy $(hk0)$ slice, and a $(1/2, k, 0)$ slice.

APPENDIX B: LINEAR SPIN WAVE FITS

In fitting the dispersions using linear spin wave theory, we extracted the mode energies at 267 unique Q points, which are plotted in the Supplemental Material [25]. The reduced χ^2 of the $Q = 0$ modes and the finite-Q spin wave modes were calculated separately and added, so that the number of points does not give undue weight to the neutron spectra.

We estimated uncertainty for the fitted exchange parameters by mapping out the reduced χ^2 contour for one standard deviation uncertainty [45]. Following the method in Ref. [46], we fixed each parameter to a value slightly above or below its best fit value and varied the other parameters until an optimum fit was achieved. If this new best fit χ^2 is within $\Delta\chi^2 = 1$ of the optimum χ^2, we keep it as a valid solution and take

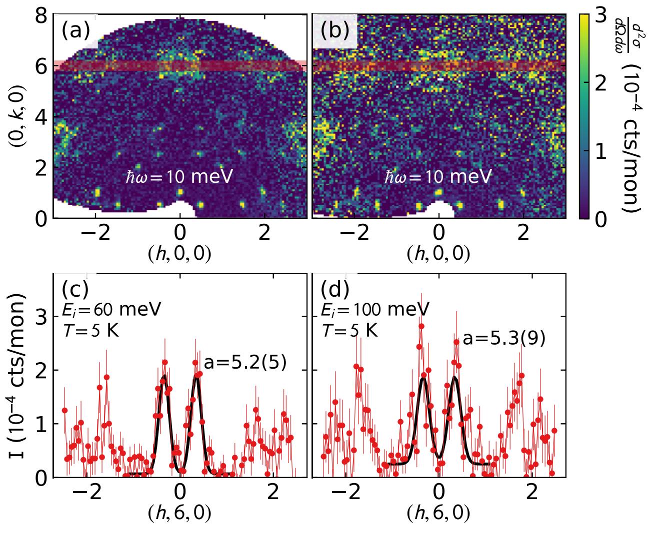

FIG. 11. Phonon fits for absolute unit conversions. Linear cuts through the $T = 5$ K (0,6,0) acoustic phonons at $\hbar\omega = 10$ meV scattering, the integrated width shown by the faint red lines in (a) and (b), at $E_i = 60$ meV (left) and $E_i = 100$ meV (right) were fitted to Gaussian curves to extract the area a in (c) and (d). This was used to normalize the scattering intensity to absolute units.

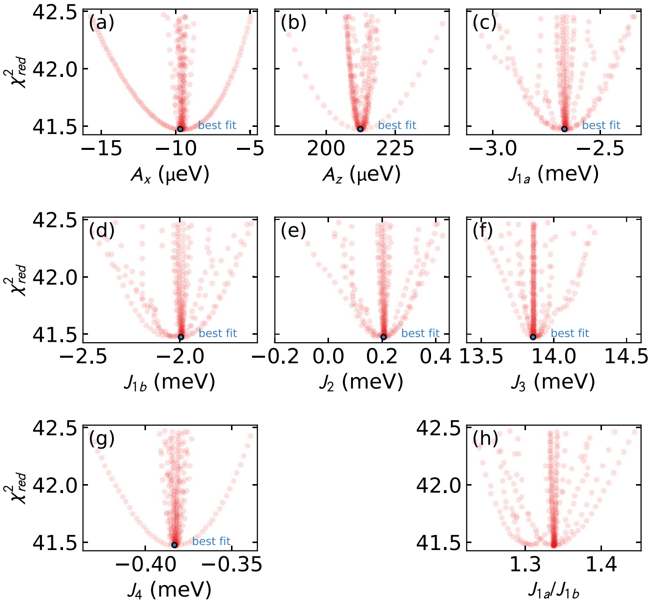

FIG. 12. Range of solutions for NiPS$_3$ spin waves within $\Delta\chi^2 = 1$ of the best fit solution, using a method of fixing a parameter and allowing all others to fit freely. This was used to determine the one standard deviation uncertainty in Table I. (h) The χ^2 contour for J_{1a}/J_{1b}, showing that although the J_{1a} and J_{1b} single-value uncertainties overlap, they are unequal to within uncertainty.

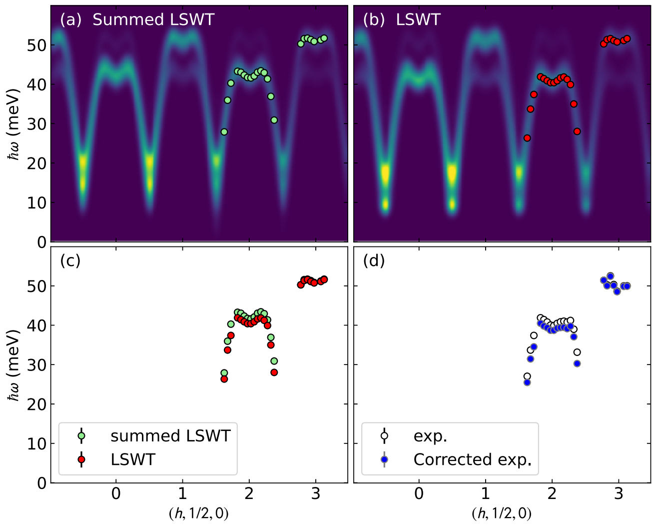

FIG. 13. Effect of finite integration window on spin wave dispersion. (a) The LSWT simulated scattering along $(h, 1/2, 0)$ summed over $-0.05 < k < 0.05$ reciprocal lattice units (RLU) and $-0.3 < \ell < 0.3$ RLU. (b) The same data at exactly $(h, 1/2, 0)$, but with Gaussian broadening applied. The colored circles give the fitted mode energies at the same wave vectors that were extracted from experiment. (c) The difference between the mode energies extracted from (a) and (b). (d) The experimental extracted mode energies (white) and the corrected mode energies (blue) shifted by the offset determined in (c).

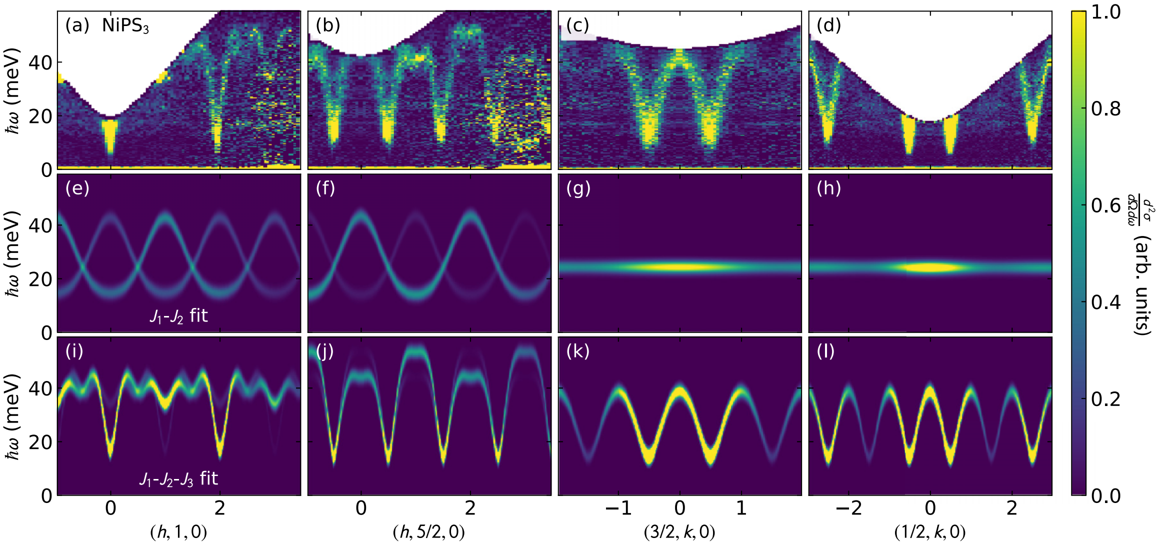

FIG. 14. Measured and fitted NiPS$_3$ spin wave spectra showing the effect of J_3. [(a)–(e)] The measured spin wave spectra. [(f)–(j)] The fitted linear spin wave theory (LSWT) spectra using a J_1-J_2 model. [(i)–(l)] The fit using a J_1-J_2-J_3 model. In none of the cuts does the J_1-J_2 model resemble the data, while the addition of J_3 makes the spin wave calculated modes match experiment much more closely.

another step away from the optimum. This is repeated until the best fit values are greater than $\Delta\chi^2 = 1$, and are no longer within one standard deviation uncertainty of the optimum. Plots of valid solutions are shown in Fig. 12. In this way, the extrema of the χ^2 contour is mapped out along every fitted variable, and the extent is taken to be a measure of statistical uncertainty.

Figure 13 shows the effect of finite width binning on the simulated LSWT data, and showing that this effect shifts the dispersions up in energy from their actual locations. In the final fits reported in the main text, the experimentally fitted spin wave modes were shifted downward in energy to account for this effect by calculating the difference between the LSWT

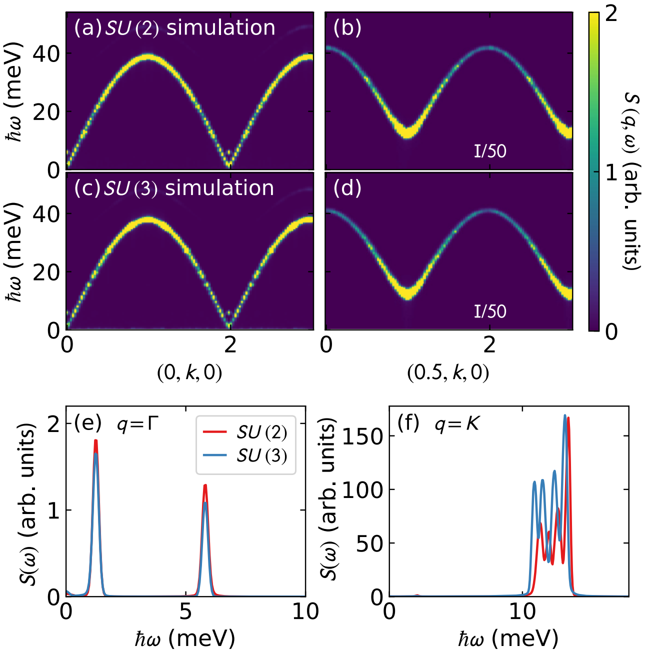

FIG. 15. Calculated NiPS$_3$ dispersion for $SU(2)$ (classical dipolar) and $SU(3)$ ($S = 1$) dynamics using Landau-Lifshitz dynamics as implemented with SU(N)NY [51]. Calculated dispersions along two different cuts for [(a), (b)] $SU(2)$ and [(c), (d)] $SU(3)$. The differences are very minor, involving only a suppression of intensity at the lowest-energy $q = \Gamma$ modes, and a slight enhancement at $q = K = (1/2, 1/2, 0)$. Thus quadrupolar $SU(3)$ dynamics does not explain the discrepancy between experiment and LSWT in Fig. 8.

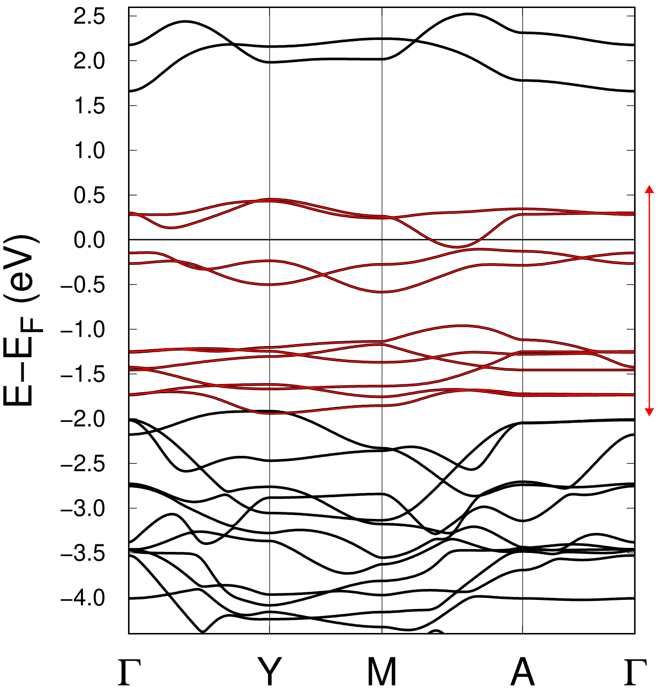

FIG. 16. Bulk band structure without spin-orbit coupling. The red bands are produced from the Wannier function Hamiltonian and the disentanglement window is depicted by the double-headed red arrow.

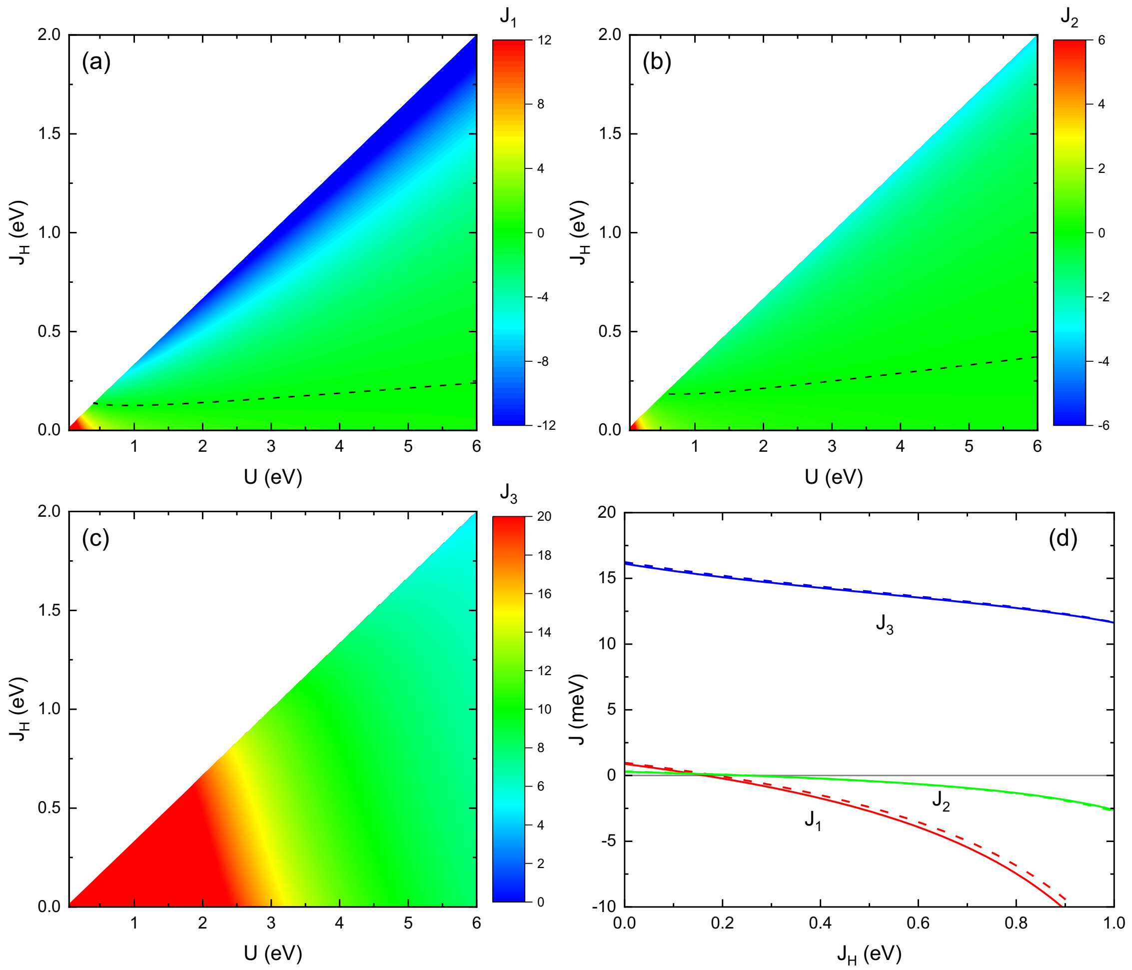

FIG. 17. Exchange constants (meV) as a function of U and J_H for (a) J_1 along the X_1 bond, (b) J_2 along the X_2 bond, and (c) J_3 along the X_3 bond. The dashed lines are the 0 meV isocurves. (d) For the specific case of $U = 3$ eV, J_1 and J_2 are FM for all but the smallest J_H. Solid lines are for $X_{1,2,3}$ bonds, and dashed lines are for $Z_{1,2,3}$ bonds.

at infinitesimal Q binning and at the actual experimental Q binning.

Effect of J_3

J_3 is by far the largest exchange interaction in the NiPS$_3$ Hamiltonian, and excluding J_3 from the fitted model worsens the fit by an order of magnitude. To visually demonstrate the effect of J_3, we plot the best fit Hamiltonians both with and without J_3 in Fig. 14. For certain cuts along k, nonzero J_3 is necessary to produce any dispersion at all, which in experiment is quite substantial. Indeed, if we force J_3 to be zero and refit (including up to J_5), we find that the best fit $\chi^2_{\rm red}$ worsens by an order of magnitude ($\chi^2_{\rm red} = 41.5$ for $J_1 - J_2 - J_3$, $\chi^2_{\rm red} = 414.9$ with $J_3 = 0$). Thus the magnitude of J_3 is well constrained by the experimental neutron scattering data.

TABLE III. Local (on-site) hopping integrals (meV).

	Local				
	d_{z^2}	$d_{x^2-y^2}$	d_{xz}	d_{yz}	d_{xy}
d_{z^2}	0.00	0.00	−2.22	−2.22	4.60
$d_{x^2-y^2}$	0.00	−17.22	−3.40	3.40	0.00
d_{xz}	−2.22	−3.40	−1339.76	53.81	46.98
d_{yz}	−2.22	3.40	53.81	−1339.76	46.98
d_{xy}	4.60	0.00	46.98	46.98	−1330.35

APPENDIX C: RESOLUTION CONVOLUTION

The instrumental resolution uses an incident beam profile calculated by Monte Carlo ray tracing in MCSTAS with GPUs [47]. This profile is then used to calculate point spread functions (PSFs) on a discrete array across the slice by using the dgsres tool in MCVINE [48]. Next the PSFs are fit to provide parameters that allow interpolation of the resolution to any point in the slice [49]. The model slice to convolute was then calculated in SPINW on a grid much finer than the resolution. Finally, the interpolated functions were used to convolute the model slice with the instrumental resolution and produce the results.

For this specific slice the incident beam energy matching the measurement of $E_i = 28.94$ meV was calculated [50]. The discrete array grid was along k from −4 to 4 in steps of 0.4

TABLE IV. Nearest-neighbor hopping integrals (meV).

	Z_1 bond					X_1 bond				
	d_{z^2}	$d_{x^2-y^2}$	d_{xz}	d_{yz}	d_{xy}	d_{z^2}	$d_{x^2-y^2}$	d_{xz}	d_{yz}	d_{xy}
d_{z^2}	−52.94	0.00	−1.97	−1.97	176.01	−21.43	17.50	66.07	−85.97	−61.37
$d_{x^2-y^2}$	0.00	−10.72	67.39	−67.39	0.00	17.50	−39.73	34.68	157.39	−36.97
d_{xz}	−1.97	67.39	45.49	13.28	34.00	66.07	34.68	42.59	36.31	19.48
d_{yz}	−1.97	−67.39	13.28	45.49	34.00	−85.97	157.39	36.31	−174.72	36.19
d_{xy}	176.01	0.00	34.00	34.00	−178.25	−61.37	−36.97	19.48	36.19	43.91

and along $\hbar\omega$ from −5 to 26 in steps of 2 meV. The model slice was over the same bounds with 2036 k bins and 1466 $\hbar\omega$ bins.

APPENDIX D: EFFECTS OF $SU(3)$ DYNAMICS

As noted in the main text, an $S = 1$ spin technically has $SU(3)$ symmetry. For weak anisotropies the $S = 1$ spin can be treated as a dipole, but as anisotropy grows, the higher-order multipolar effects become more manifest, which allows a single-site spin singlet ($S = 0$) state [40]. To simulate the effects of this in NiPS$_3$, we calculated the inelastic neutron scattering spectrum using the generalized spin wave package SU(N)NY software suite [51] using Landau-Lifshitz dynamics [52] on a 75 × 75 × 4 supercell at $T = 5$ K using the fitted Hamiltonian in Table I. [In $SU(3)$ simulations the anisotropy was multiplied by 2 to keep the spin wave gaps at Γ the same as in $SU(2)$.] Both the $SU(3)$ and $SU(2)$ results are shown in Fig. 15. Note that the simulations in Fig. 15 do not include the effects of finite momentum space resolution.

The simulated $SU(3)$ and $SU(2)$ spectra are nearly identical, involving only a weak 14% suppression of low-energy intensity from higher-order $SU(3)$ effects. If we normalize the low-energy intensity relative to the 10–15 meV modes from $q = K$ (which practically speaking is what is done in Fig. 8), we find a suppression of 39% in $SU(3)$ intensity relative to $SU(2)$. This is a mild reduction in intensity, but nowhere near as much as would be required to explain the absent intensity in Fig. 8. This means that the reduced low-energy intensity, alongside the reduced static magnetic moment, requires a more exotic explanation.

APPENDIX E: FIRST-PRINCIPLES CALCULATIONS

We perform density functional theory (DFT) calculations as implemented in VASP [53,54]. The calculations are performed within the Perdew-Burke-Ernzerhof (PBE) generalized gradient approximation (GGA) [55] for the exchange-correlation functional without spin-orbit coupling. We use projector augmented wave (PAW) pseudopotentials [56,57] with an energy cutoff of 300 eV and an 11 × 11 × 9 Monkhorst-Pack k-point mesh. We adopt the experimental lattice constants of Wildes [5] for $C2/m$ bulk NiPS$_3$ and relax the atomic positions until component forces are less than 1 meV/Å. We use WANNIER90 [58–60] to create a tight-binding Hamiltonian by projecting the band structure onto real Ni d orbitals. The maximal-localization step is not performed in order to maintain the symmetry of the Wannier functions close to their centers. The disentanglement window is shown by the double-headed arrow in Fig. 16(a) and the disentanglement convergence criterion is set to 10^{-13} Å^2. The resulting Hamiltonian is ensured to be symmetrized by postprocessing with WANNSYMM [61].

The global Cartesian coordinate system was chosen such that the projection of the z axis onto the Ni plane is perpendicular to the Z_1 bond [62]. Explicitly, the primitive lattice row vectors for this choice of axes are

$$\begin{aligned}\vec{a} &= (-2.3932999259, \quad 4.7774699422, -2.3841700163),\\ \vec{b} &= (-4.7774699422, \quad 2.3932999259, \quad 2.3841700163),\\ \vec{c} &= (2.8698582203, \quad 2.8698582203, \quad 5.2691203152),\end{aligned} \tag{E1}$$

in units of Å.

Figure 16 shows the excellent agreement between the electronic band structure calculated with DFT and the Wannier tight-binding model for the Ni d orbitals. We accurately capture the e_g bands near the Fermi level and the lower t_{2g} bands.

To carry out the second-order perturbation calculation, the single-particle Hamiltonian as parametrized by a Wannier tight-binding model is supplemented by a local Coulomb

TABLE V. Second-nearest-neighbor hopping integrals (meV).

	Z_2 bond					X_2 bond				
	d_{z^2}	$d_{x^2-y^2}$	d_{xz}	d_{yz}	d_{xy}	d_{z^2}	$d_{x^2-y^2}$	d_{xz}	d_{yz}	d_{xy}
d_{z^2}	29.54	3.25	−43.37	4.04	67.06	3.58	−12.56	27.18	−51.42	−3.02
$d_{x^2-y^2}$	−3.25	−5.17	26.69	−31.79	19.83	−17.29	19.47	15.87	46.52	−48.79
d_{xz}	4.04	31.79	5.15	−44.68	9.16	46.00	−22.06	5.20	11.64	20.57
d_{yz}	−43.37	−26.69	18.10	5.15	11.79	−17.11	70.16	7.20	−2.98	12.50
d_{xy}	67.06	−19.83	11.79	9.16	−3.50	−28.69	−14.71	−42.31	8.83	4.80

TABLE VI. Third-nearest-neighbor hopping integrals (meV).

	Z_3 bond					X_3 bond				
	d_{z^2}	$d_{x^2-y^2}$	d_{xz}	d_{yz}	d_{xy}	d_{z^2}	$d_{x^2-y^2}$	d_{xz}	d_{yz}	d_{xy}
d_{z^2}	−47.60	0.00	2.19	2.19	72.99	152.31	111.35	−6.38	−35.50	5.70
$d_{x^2-y^2}$	0.00	215.52	−9.11	−9.11	0.00	111.35	18.54	−0.69	62.54	5.44
d_{xz}	2.19	−9.11	12.03	−11.18	−5.21	−6.38	−0.69	11.03	−4.02	−10.72
d_{yz}	2.19	−9.11	−11.18	12.03	−5.21	−35.50	62.54	−4.02	31.64	−6.26
d_{xy}	72.99	0.00	−5.21	−5.21	32.74	5.70	5.44	−10.72	−6.26	11.37

interaction Hamiltonian given by

$$\begin{aligned} H_U = {} & U \sum_{\alpha} d^\dagger_{\alpha\uparrow} d_{\alpha\uparrow} d^\dagger_{\alpha\downarrow} d_{\alpha\downarrow} + U' \sum_{\alpha\neq\beta} d^\dagger_{\alpha\uparrow} d_{\alpha\uparrow} d^\dagger_{\beta\downarrow} d_{\beta\downarrow} \\ & + (U' - J_H) \sum_{\alpha>\beta,\sigma} d^\dagger_{\alpha\sigma} d_{\alpha\sigma} d^\dagger_{\beta\sigma} d_{\beta\sigma} \\ & + J_H \sum_{\alpha\neq\beta} (d^\dagger_{\alpha\uparrow} d_{\beta\uparrow} d^\dagger_{\beta\downarrow} d_{\alpha\downarrow} + d^\dagger_{\alpha\uparrow} d_{\beta\uparrow} d^\dagger_{\alpha\downarrow} d_{\beta\downarrow}), \end{aligned} \tag{E2}$$

where α and β label $(yz, zx, xy, z^2, x^2 - y^2)$ at the Ni d shell, and $d^{(\dagger)}_{\alpha\sigma}$ is the annihilation (creation) operator of an electron at orbital α with spin σ. U and U' are the intraorbital Coulomb interaction and the interorbital Coulomb interaction, respectively, and J_H represents the interorbital exchange interaction, i.e., the Hund coupling (fourth term), and the interorbital pair hopping (fifth term). Between three parameters, we assume $U' = U - 2J_H$ [63]. Because the energy scale of U is order of eV, while that of the off-diagonal and anisotropic terms in the crystal field is smaller than 0.1 eV, except for the level difference between e_g and t_{2g} multiplets, known as $10Dq$, we only consider $10Dq$ by averaging e_g and t_{2g} levels,

$$H_{CF} = 10Dq \sum_{\alpha\in e_g,\sigma} d^\dagger_{\alpha\sigma} d_{\alpha\sigma}, \tag{E3}$$

with the average t_{2g} level set to zero. The relativistic spin-orbit coupling is not included for simplicity.

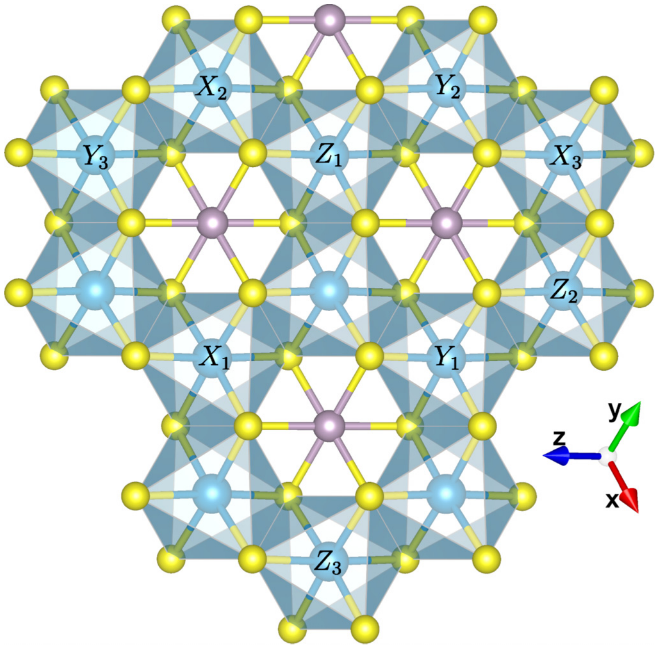

FIG. 18. In-plane atoms to which the hopping integrals of Tables IV, V, and VI refer.

By diagonalizing $H_{CF} + H_U$ with d^8 configurations for the Ni^{2+} ion, we obtain the high-spin $e_g^2 t_{2g}^6$ ground state. From a pair of such high-spin $e_g^2 t_{2g}^6$ states, we proceed to carry out second-order perturbation calculations with respect to intersite electron hopping between Ni sites. Here, we consider two magnetic sites with ferromagnetic spin alignment (E_{FM}) and antiferromagnetic alignment (E_{AFM}) and compute the second-order correction to the ground-state energy. During this process, all excited states for d^7 and d^9 configurations are included by diagonalizing $H_{CF} + H_U$. Finally, considering the full spin rotational symmetry, an exchange constant at a given pair of Ni spins is given by $J = (E_{FM} - E_{AFM})/2$. Figure 17 shows the exchange constants as a function of U and J_H for various parameters, and Tables III, IV, V, and VI show the hopping integrals for the on-site through third-neighbor interactions (Fig. 18).

---

[1] K. S. Burch, D. Mandrus, and J.-G. Park, Magnetism in two-dimensional van der Waals materials, Nature (London) **563**, 47 (2018).

[2] K. Momma and F. Izumi, VESTA3 for three-dimensional visualization of crystal, volumetric and morphology data, J. Appl. Crystallogr. **44**, 1272 (2011).

[3] P. A. Joy and S. Vasudevan, Magnetism in the layered transition-metal thiophosphates MPS$_3$ (M = Mn, Fe, and Ni), Phys. Rev. B **46**, 5425 (1992).

[4] G. Le Flem, R. Brec, G. Ouvard, A. Louisy, and P. Segransan, Magnetic interactions in the layer compounds MPX_3 (M = Mn, Fe, Ni; X = S, Se), J. Phys. Chem. Solids **43**, 455 (1982).

[5] A. R. Wildes, V. Simonet, E. Ressouche, G. J. McIntyre, M. Avdeev, E. Suard, S. A. J. Kimber, D. Lançon, G. Pepe, B. Moubaraki, and T. J. Hicks, Magnetic structure of the quasi-two-dimensional antiferromagnet NiPS$_3$, Phys. Rev. B **92**, 224408 (2015).

[6] S. Y. Kim, T. Y. Kim, L. J. Sandilands, S. Sinn, M.-C. Lee, J. Son, S. Lee, K.-Y. Choi, W. Kim, B.-G. Park, C. Jeon, H.-D. Kim, C.-H. Park, J.-G. Park, S. J. Moon, and T. W. Noh, Charge-Spin Correlation in van der Waals Antiferromagnet NiPS$_3$, Phys. Rev. Lett. **120**, 136402 (2018).

[7] D. Afanasiev, J. R. Hortensius, M. Matthiesen, S. Mañas-Valero, M. Šiškins, M. Lee, E. Lesne, H. S. van Der Zant, P. G.

Steeneken, B. A. Ivanov *et al.*, Controlling the anisotropy of a van der Waals antiferromagnet with light, Sci. Adv. **7**, eabf3096 (2021).

[8] R. N. Jenjeti, R. Kumar, M. P. Austeria, and S. Sampath, Field effect transistor based on layered $NiPS_3$, Sci. Rep. **8**, 8586 (2018).

[9] J. Liu, X. Li, Y. Xu, Y. Ge, Y. Wang, F. Zhang, Y. Wang, Y. Fang, F. Yang, C. Wang *et al.*, $NiPS_3$ nanoflakes: A nonlinear optical material for ultrafast photonics, Nanoscale **11**, 14383 (2019).

[10] D. Lançon, R. A. Ewings, T. Guidi, F. Formisano, and A. R. Wildes, Magnetic exchange parameters and anisotropy of the quasi-two-dimensional antiferromagnet $NiPS_3$, Phys. Rev. B **98**, 134414 (2018).

[11] A. R. Wildes, J. R. Stewart, M. D. Le, R. A. Ewings, K. C. Rule, G. Deng, and K. Anand, Magnetic dynamics of $NiPS_3$, Phys. Rev. B **106**, 174422 (2022).

[12] T. Olsen, Magnetic anisotropy and exchange interactions of two-dimensional $FePS_3$, $NiPS_3$ and $MnPS_3$ from first principles calculations, J. Phys. D **54**, 314001 (2021).

[13] M. Mi, X. Zheng, S. Wang, Y. Zhou, L. Yu, H. Xiao, H. Song, B. Shen, F. Li, L. Bai, Y. Chen, S. Wang, X. Liu, and Y. Wang, Variation between antiferromagnetism and ferrimagnetism in $NiPS_3$ by electron doping, Adv. Funct. Mater. **32**, 2112750 (2022).

[14] S. Kang, K. Kim, B. H. Kim, J. Kim, K. I. Sim, J.-U. Lee, S. Lee, K. Park, S. Yun, T. Kim, A. Nag, A. Walters, M. Garcia-Fernandez, J. Li, L. Chapon, K.-J. Zhou, Y.-W. Son, J. H. Kim, H. Cheong, and J.-G. Park, Coherent many-body exciton in van der Waals antiferromagnet $NiPS_3$, Nature (London) **583**, 785 (2020).

[15] G. E. Granroth, D. H. Vandergriff, and S. E. Nagler, Sequoia: A fine resolution chopper spectrometer at the SNS, Phys. B: Condens. Matter **385-386**, 1104 (2006).

[16] G. E. Granroth, A. I. Kolesnikov, T. E. Sherline, J. P. Clancy, K. A. Ross, J. P. C. Ruff, B. D. Gaulin, and S. E. Nagler, SEQUOIA: A newly operating chopper spectrometer at the SNS, J. Phys.: Conf. Ser. **251**, 012058 (2010).

[17] T. E. Mason, D. Abernathy, I. Anderson, J. Ankner, T. Egami, G. Ehlers, A. Ekkebus, G. Granroth, M. Hagen, K. Herwig, J. Hodges, C. Hoffmann, C. Horak, L. Horton, F. Klose, J. Larese, A. Mesecar, D. Myles, J. Neuefeind, M. Ohl *et al.*, The Spallation Neutron Source in Oak Ridge: A powerful tool for materials research, Phys. B: Condens. Matter **385-386**, 955 (2006).

[18] K. Nagata and Y. Tomono, Antiferromagnetic resonance frequency in quadratic layer antiferromagnets, J. Phys. Soc. Jpn. **36**, 78 (1974).

[19] A. R. Wildes, K. C. Rule, R. I. Bewley, M. Enderle, and T. J. Hicks, The magnon dynamics and spin exchange parameters of $FePS_3$, J. Phys.: Condens. Matter **24**, 416004 (2012).

[20] A. Wildes, H. Rønnow, B. Roessli, M. Harris, and K. Godfrey, Anisotropy and the critical behaviour of the quasi-2D antiferromagnet, $MnPS_3$, J. Magn. Magn. Mater. **310**, 1221 (2007).

[21] K. Kim, S. Y. Lim, J.-U. Lee, S. Lee, T. Y. Kim, K. Park, G. S. Jeon, C.-H. Park, J.-G. Park, and H. Cheong, Suppression of magnetic ordering in XXZ-type antiferromagnetic monolayer $NiPS_3$, Nat. Commun. **10**, 345 (2019).

[22] K. Mehlawat, A. Alfonsov, S. Selter, Y. Shemerliuk, S. Aswartham, B. Büchner, and V. Kataev, Low-energy excitations and magnetic anisotropy of the layered van der Waals antiferromagnet $Ni_2P_2S_6$, Phys. Rev. B **105**, 214427 (2022).

[23] C. A. Belvin, E. Baldini, I. O. Ozel, D. Mao, H. C. Po, C. J. Allington, S. Son, J. Kim, Beom Hyunand Kim, I. Hwang, J. H. Kim, T. Park, Je-Geunand Senthil, and N. Gedik, Exciton-driven antiferromagnetic metal in a correlated van der Waals insulator, Nat. Commun. **12**, 4837 (2021).

[24] I. Affleck, Model for Quasi-one-Dimensional Antiferromagnets: Application to $CsNiCl_3$, Phys. Rev. Lett. **62**, 474 (1989).

[25] See Supplemental Material at http://link.aps.org/supplemental/10.1103/PhysRevB.108.104402 for more details of the experiments and calculations.

[26] S. Toth and B. Lake, Linear spin wave theory for single-Q incommensurate magnetic structures, J. Phys.: Condens. Matter **27**, 166002 (2015).

[27] K. Takubo, T. Mizokawa, J.-Y. Son, Y. Nambu, S. Nakatsuji, and Y. Maeno, Unusual Superexchange Pathways in an NiS_2 Triangular Lattice with Negative Charge-Transfer Energy, Phys. Rev. Lett. **99**, 037203 (2007).

[28] S. Asai, M. Soda, K. Kasatani, T. Ono, V. O. Garlea, B. Winn, and T. Masuda, Spin dynamics in the stripe-ordered buckled honeycomb lattice antiferromagnet Ba_2NiTeO_6, Phys. Rev. B **96**, 104414 (2017).

[29] W. Yao, K. Iida, K. Kamazawa, and Y. Li, Excitations in the Ordered and Paramagnetic States of Honeycomb Magnet $Na_2Co_2TeO_6$, Phys. Rev. Lett. **129**, 147202 (2022).

[30] B. Gao, T. Chen, C. Wang, L. Chen, R. Zhong, D. L. Abernathy, D. Xiao, and P. Dai, Spin waves and Dirac magnons in a honeycomb-lattice zigzag antiferromagnet $BaNi_2(AsO_4)_2$, Phys. Rev. B **104**, 214432 (2021).

[31] T. Halloran, F. Desrochers, E. Z. Zhang, T. Chen, L. E. Chern, Z. Xu, B. Winn, M. Graves-Brook, M. B. Stone, A. I. Kolesnikov, Y. Qiu, R. Zhong, R. Cava, Y. B. Kim, and C. Broholm, Geometrical frustration versus Kitaev interactions in $BaCo_2(AsO_4)_2$, Proc. Natl. Acad. Sci. USA **120**, e2215509119 (2023).

[32] B. L. Chittari, Y. Park, D. Lee, M. Han, A. H. MacDonald, E. Hwang, and J. Jung, Electronic and magnetic properties of single-layer MPX_3 metal phosphorous trichalcogenides, Phys. Rev. B **94**, 184428 (2016).

[33] Y. Sugita, T. Miyake, and Y. Motome, Multiple Dirac cones and topological magnetism in honeycomb-monolayer transition metal trichalcogenides, Phys. Rev. B **97**, 035125 (2018).

[34] C. Kim, J. Jeong, P. Park, T. Masuda, S. Asai, S. Itoh, H.-S. Kim, A. Wildes, and J.-G. Park, Spin waves in the two-dimensional honeycomb lattice XXZ-type van der Waals antiferromagnet $CoPS_3$, Phys. Rev. B **102**, 184429 (2020).

[35] N. Sivadas, M. W. Daniels, R. H. Swendsen, S. Okamoto, and D. Xiao, Magnetic ground state of semiconducting transition-metal trichalcogenide monolayers, Phys. Rev. B **91**, 235425 (2015).

[36] J. M. Ziman, *Principles of the Theory of Solids* (Cambridge University Press, Cambridge, U.K., 1972).

[37] A. Scheie, P. Laurell, A. M. Samarakoon, B. Lake, S. E. Nagler, G. E. Granroth, S. Okamoto, G. Alvarez, and D. A. Tennant, Witnessing entanglement in quantum magnets using neutron scattering, Phys. Rev. B **103**, 224434 (2021).

[38] J. Y. Y. Lin, F. Islam, G. Sala, I. Lumsden, H. Smith, M. Doucet, M. B. Stone, D. L. Abernathy, G. Ehlers, J. F. Ankner, and G. E.

Granroth, Recent developments of MCVINE and its applications at SNS, J. Phys. Commun. **3**, 085005 (2019).

[39] J. Y. Lin, H. L. Smith, G. E. Granroth, D. L. Abernathy, M. D. Lumsden, B. Winn, A. A. Aczel, M. Aivazis, and B. Fultz, MCVINE - an object oriented Monte Carlo neutron ray tracing simulation package, Nucl. Instrum. Methods Phys. Res., Sect. A **810**, 86 (2016).

[40] H. Zhang and C. D. Batista, Classical spin dynamics based on SU(n) coherent states, Phys. Rev. B **104**, 104409 (2021).

[41] K. C. Rule, R. A. Mole, and D. Yu, Which glue to choose? A neutron scattering study of various adhesive materials and their effect on background scattering, J. Appl. Crystallogr. **51**, 1766 (2018).

[42] C. Murayama, M. Okabe, D. Urushihara, T. Asaka, K. Fukuda, M. Isobe, K. Yamamoto, and Y. Matsushita, Crystallographic features related to a van der Waals coupling in the layered chalcogenide $\mathrm{FePS_3}$, J. Appl. Phys. **120**, 142114 (2016).

[43] D. Lançon, H. C. Walker, E. Ressouche, B. Ouladdiaf, K. C. Rule, G. J. McIntyre, T. J. Hicks, H. M. Rønnow, and A. R. Wildes, Magnetic structure and magnon dynamics of the quasi-two-dimensional antiferromagnet $\mathrm{FePS_3}$, Phys. Rev. B **94**, 214407 (2016).

[44] G. Xu, Z. Xu, and J. M. Tranquada, Absolute cross-section normalization of magnetic neutron scattering data, Rev. Sci. Instrum. **84**, 083906 (2013).

[45] W. H. Press, S. A. Teukolsky, W. T. Vetterling, and B. P. Flannery, *Numerical Recipes 3rd Edition: The Art of Scientific Computing* (Cambridge University Press, Cambridge, U.K., 2007).

[46] A. Scheie, P. Laurell, P. A. McClarty, G. E. Granroth, M. B. Stone, R. Moessner, and S. E. Nagler, Spin-exchange Hamiltonian and topological degeneracies in elemental gadolinium, Phys. Rev. B **105**, 104402 (2022).

[47] P. K. Willendrup and K. Lefmann, MCSTAS (i): Introduction, use, and basic principles for ray-tracing simulations, J. Neutron Res. **22**, 1 (2020).

[48] J. Y. Y. Lin, F. Islam, and G. E. Granroth, mcvine/dgsres: Version 0.2, Zenodo (2021), doi:10.5281/zenodo.5137820.

[49] J. Y. Y. Lin, G. Sala, and M. B. Stone, A super-resolution technique to analyze single-crystal inelastic neutron scattering measurements using direct-geometry chopper spectrometers, Rev. Sci. Instrum. **93**, 025101 (2022).

[50] G. E. Granroth, W. Zhou, M. B. Stone, and A. I. Kolesnikov (unpublished).

[51] D. Dahlbom, H. Zhang, C. Miles, X. Bai, C. D. Batista, and K. Barros, SU(N)NY, https://github.com/SunnySuite/Sunny.jl.

[52] D. Dahlbom, C. Miles, H. Zhang, C. D. Batista, and K. Barros, Langevin dynamics of generalized spins as SU(n) coherent states, Phys. Rev. B **106**, 235154 (2022).

[53] G. Kresse and J. Furthmüller, Efficient iterative schemes for *ab initio* total-energy calculations using a plane-wave basis set, Phys. Rev. B **54**, 11169 (1996).

[54] G. Kresse and J. Furthmüller, Efficiency of ab-initio total energy calculations for metals and semiconductors using a plane-wave basis set, Comput. Mater. Sci. **6**, 15 (1996).

[55] J. P. Perdew, K. Burke, and M. Ernzerhof, Generalized Gradient Approximation Made Simple, Phys. Rev. Lett. **77**, 3865 (1996).

[56] P. E. Blöchl, Projector augmented-wave method, Phys. Rev. B **50**, 17953 (1994).

[57] G. Kresse and D. Joubert, From ultrasoft pseudopotentials to the projector augmented-wave method, Phys. Rev. B **59**, 1758 (1999).

[58] A. A. Mostofi, J. R. Yates, G. Pizzi, Y.-S. Lee, I. Souza, D. Vanderbilt, and N. Marzari, An updated version of WANNIER90: A tool for obtaining maximally-localised Wannier functions, Comput. Phys. Commun. **185**, 2309 (2014).

[59] N. Marzari and D. Vanderbilt, Maximally localized generalized Wannier functions for composite energy bands, Phys. Rev. B **56**, 12847 (1997).

[60] I. Souza, N. Marzari, and D. Vanderbilt, Maximally localized Wannier functions for entangled energy bands, Phys. Rev. B **65**, 035109 (2001).

[61] G.-X. Zhi, C.-C. Xu, S.-Q. Wu, F.-L. Ning, and C. Cao, WANNSYMM: A symmetry analysis code for Wannier orbitals, Comput. Phys. Commun. **271**, 108196 (2022).

[62] S. M. Winter, Y. Li, H. O. Jeschke, and R. Valentí, Challenges in design of Kitaev materials: Magnetic interactions from competing energy scales, Phys. Rev. B **93**, 214431 (2016).

[63] J. Kanamori, Electron correlation and ferromagnetism of transition metals, Prog. Theor. Phys. **30**, 275 (1963).